remote sensing

MDPI

Article

Study on Local Power Plant Emissions Using Multi-Frequency Differential Absorption LIDAR and Real-Time Plume Tracking

Jasper R. Stroud [1,*], William J. Dienstfrey [2] and David F. Plusquellic [1]

[1] Applied Physics Division, Physical Measurement Laboratory, National Institute of Standards and Technology, Boulder, CO 80305, USA; david.plusquellic@nist.gov
[2] Department of Physics, Amherst College, Amherst, MA 01002, USA; wdienstfrey24@amherst.edu
* Correspondence: jasper.stroud@nist.gov

Abstract: We present a new fiber-amplifier-based differential absorption light detection and ranging (DIAL) system for range-resolved detection of carbon dioxide (CO_2) and water vapor (H_2O) over a range of a few kilometers. The fiber amplifier chain is seeded with a 7.14 kHz fast-switching high-spectral purity wavelength source near 1572 nm to cover ten different frequencies across the CO_2/H_2O line pair in ≈1.4 ms. We demonstrate the system in a study of CO_2 emissions from a local power plant in Boulder, CO, USA. We use real-time wind information to predict the plume location for tracking and modeling of the CO_2 emission rate to compare with the reported data from the power plant over a 13 h period. There is overall agreement with the reported burn rate, but we see periods of bias towards underestimation of the CO_2 emission rate. We attribute the dropout periods to uncertainties between the measured and the plant's local wind speed data that impact both the tracking location and the plume model predictions. Upcoming studies that will make use of real-time Doppler wind data are expected to significantly decrease these uncertainties.

Keywords: differential absorption LIDAR; remote sensing; greenhouse gas sensing

Citation: Stroud, J.R.; Dienstfrey, W.J.; Plusquellic, D.F. Study on Local Power Plant Emissions Using Multi-Frequency Differential Absorption LIDAR and Real-Time Plume Tracking. *Remote Sens.* **2023**, *15*, 4283. https://doi.org/10.3390/rs15174283

Academic Editor: Carmine Serio

Received: 19 July 2023
Revised: 25 August 2023
Accepted: 29 August 2023
Published: 31 August 2023

1. Introduction

With the ever-increasing impact of climate change, new technology is needed to help monitor greenhouse gas (GHG) emissions, such as CO_2 and H_2O. Point sensors provide a weak link to remote sensing of these gases, and column-integrated measurements are only able to paint a partial picture when it comes to understanding CO_2 sources and sinks [1]. Differential absorption LIDAR (light detection and ranging, or DIAL) uses two or more LIDAR returns of the on- and off-resonance regions of an absorption line to obtain range-resolved GHG concentrations [2–4]. DIAL provides information not easily obtainable from other open-path techniques that provide column-integrated information, since range-resolved measurements enable direct construction of three-dimensional GHG concentration maps. These maps allow for a more in-depth understanding of atmospheric variations and a better quantification of GHG sources and sinks.

Emissions from power plants are ubiquitous examples of localized GHG sources. The process of burning natural gas to produce heat produces CO_2 and H_2O as waste products. The actual GHG concentrations located downwind from the source depend on local wind, temperature, atmospheric stability, and ambient levels. This variability makes it extremely difficult to track and quantify downstream CO_2 emission flux using static point sensors. Traditional flux estimates use large-scale networks of balloons, towers, and mobile point sensors but suffer from large spatial resolutions, making it difficult to accurately quantify local emissions [5,6]. Similarly, optical techniques, such as tunable absorption or Fourier transform infrared (FTIR) spectroscopy, require hard targets at multiple locations around the plume to measure flux [7,8]. A prior proof-of-concept measurement using a DIAL system in an industrial setting reported an increase in CO_2 at the plume but lacked

sufficient local meteorological data to model flux [9]. Most recently, DIAL and Doppler LIDAR systems have been combined to provide simultaneous concentration and wind information to determine plume emission flux [10]. Using two-point DIAL and a high-efficiency superconducting nanowire detector, they showed increased CO_2 flux over the industrial park compared to a local park. Here, for the first time, we apply our novel ten-point, range-resolved DIAL measurements [11] with Gaussian plume modeling using local meteorological data to estimate the emission flux of CO_2 from a point source in an urban environment.

In this work, we present a fiber-amplifier-based DIAL system for performing standoff detection of CO_2 and H_2O concentrations over a 3 km range. The compact fiber-based components make the system ideal for deployment as a mobile platform for measurements at remote locations. In contrast to previous results demonstrated with a low-pulse-rate-frequency (PRF) free-space amplifier [12], the high-PRF (5 kHz to 10 kHz) DIAL system demonstrated here takes advantage of a low-dark-count photomultiplier tube (PMT) and a high-throughput detection system with near-continuous acquisition of returns. We demonstrate the DIAL system to observe the dry-air CO_2 concentrations from a local power plant's stack emissions located at a distance of 1.13 km. Wind sensor data sampled above the lab are used in a Gaussian plume model to determine the pointing direction of the transceiver in real time to maximize overlap between the DIAL beam and the plume center. Finally, we use models to compare the observed increase in CO_2 concentrations to the reported natural gas burn rate from the University of Colorado (CU) East District Energy Plant (EDEP) power plant [13].

In Section 2.1, we give a description of the DIAL instrument including the fast frequency switching seed source and pulse generator. In Section 2.2, the method for plume modeling and tracking is discussed. In Section 2.3, we discuss the methods and approximations used to compare the DIAL-based emission rate with natural gas burn rate.

2. Materials and Methods

2.1. DIAL System

A schematic of the overall system is shown in Figure 1, and specifications of the components are given in Table 1. The frequency converter begins with a single, fiber-coupled, external-cavity diode laser (ECDL). The output is 90/10% split, where the 10% leg is frequency-offset in an acousto-optic modulator (AOM) fiber-coupled to an electro-optic phase modulator (EOM_1) and is then free-space-coupled to an Invar confocal filter cavity that is used in reflection to frequency-lock the laser (the PDH method) [12]. The 90% leg is sent to a second broadband modulator (EOM_2) that is driven by an arbitrary waveform generator (AWG). The frequencies and amplitudes of the AWG waveform are defined such that only one of the second-order comb teeth from among the generated sidebands and carrier is transmitted through the cavity [12] at any given time when modulated by a single-tone waveform. The output frequencies from the filter cavity are sequentially scanned over ten different tones every 140 µs to give a 7.14 kHz PRF. The spectral coverage is 48 GHz and probes the region containing the CO_2 line at 1572.335 nm (6359.97 cm^{-1}) and the H_2O line at 1572.257 nm (6360.28 cm^{-1}). As shown in Figure 1b, five points are selected on the CO_2 line (blue trace), one point on the H_2O line (red trace), and the remaining four points sample the background regions at both ends of the spectrum. By selecting five points across the top of the CO_2 line, we maintain a nearly equivalent signal-to-noise ratio (SNR) as in two-point DIAL and can use the line shape to fit the laser frequency [11,12]. For a range resolution of 250 m, determined by our bin size, the fractional absorption is near 4% for ambient levels (≈420 ppm) of CO_2.

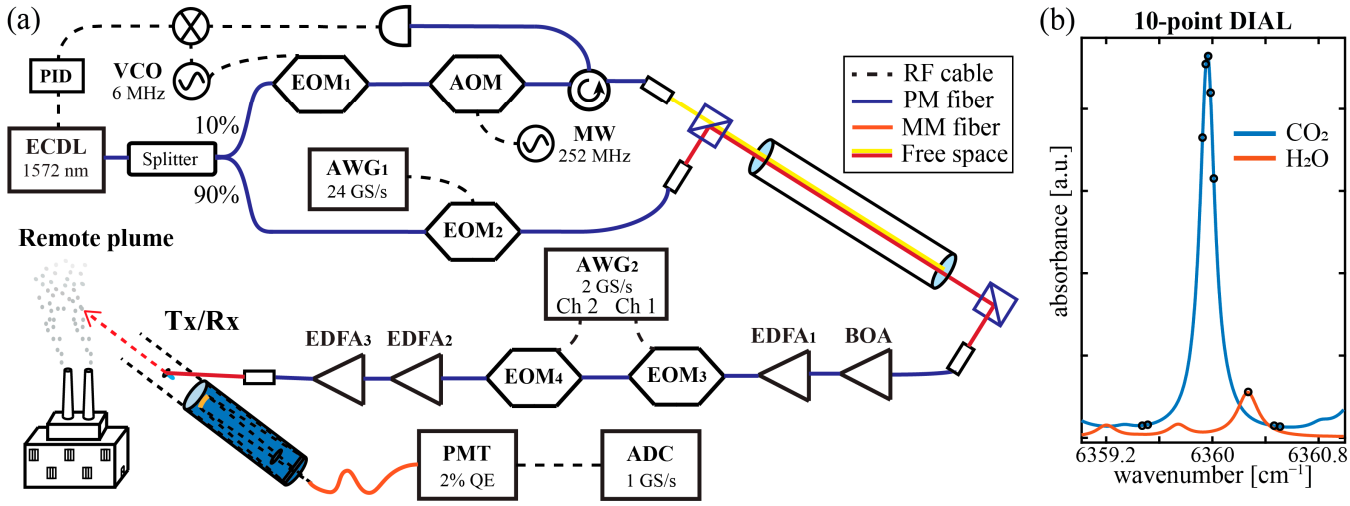

Figure 1. (**a**) A schematic of the frequency converter and transceiver system (VCO: voltage-controlled oscillator, MW: microwave source, PID: proportional–integral–differential controller, ADC: analog-to-digital converter; see Table 1). (**b**) Ten frequencies are generated (black dots) in the spectral region investigated to obtain the range-resolved CO_2 (blue simulation) and H_2O (red simulation) concentrations.

Table 1. Specifications [14] of the CO_2/H_2O fiber-amplifier-based DIAL system with a coaxial transceiver arrangement.

Frequency Converter:		
Center wavelength	1571.9 nm	New Focus, ECDL
Arbitrary waveform generator	2 GS/s, 250 MHz bandwidth	AWG_1, Tektronix, Model 3252
Electro-optic modulator	10 GHz bandwidth	EOM_1, Thorlabs
Acousto-optic modulator	252 MHz	Brimrose
Arbitrary waveform generator	24 GS/s, 8 bits, 1 channel	AWG_2, Tektronix, Model 7122C
Electro-optic modulator	20 GHz bandwidth	EOM_2, EOSpace
Electro-optic switches	1 ns speed, 40 dB isolation	EOM_3 + EOM_4, EOSpace
Invar filter cavity	300 MHz free spectral range	Burleigh, CFP-500, l = 0.5 m
Number of frequencies	10	$\Delta\nu$ = 48 GHz
Spectral purity	>99.9%	Filter cavity finesse $\approx$ 500
Booster optical amplifier	20 mW, <20 dB gain	Thorlabs, Model S9FC1082P
$EDFA_1$	100 mW, <30 dB gain	Amonics, AMN-EDFA-L01/PM
$EDFA_2$ + $EDFA_3$	105 µJ/pulse, 1 W power	NP Photonics, Custom model
Pulse length	300 ns	
Spectral linewidth	<1 MHz	Full width at half maximum
Pulse repetition rate	7.143 kHz	5 kHz to 10 kHz
Tx/Rx optics:		
Tx beam diameter	41 mm	×10 beam expansion
Tx beam M^2	<1.5	NP Photonics, Custom model
Tx beam divergence	<300 µrad	
Elevation	1.6 degrees	
Rx telescope diameter	279.4 mm	Schmidt-Cassegrain, Celestron
Bandpass filter	1.9 nm (FWHM)	>5 OD rejection, Alluxa
Neutral density filter	0.1, 0.3, 0.6, and 1 OD	Thorlabs
Fiber-coupled	300 µm aperture	1 m cable length
PMT detection	~2% QE	Hamamatsu H12397-75
Data acquisition:		
Transimpedance amp gain	5 kV/A, $\tau_{3dB} \approx$ 1 ns	Femto HCA-400M-5K-C
Digitizer	12 bits, 1 GS/s, 2 channels	GaGe EON CSE123G2
Raw data storage	10 s accumulation	NetCDF4 file format
Range resolution	250 m to 500 m	Defined in post-processing
Temporal resolution	5 min	Defined in post-processing

The output of the fast-switching wavelength source is amplitude-modulated ($\Delta t \approx 10$ μs) in a booster optical amplifier (BOA). The pulsed output is further amplified in an erbium-doped fiber amplifier (EDFA) and coupled through two EOM-based polarization switches to generate 300 ns pulses with >40 dB rejection. The fast-switching wavelength source is sent sequentially through two additional EDFA stages ($EDFA_1$ + $EDFA_2$), where the final amplifier is doped to reduce stimulated Brillouin scattering. The final amplifier beam is specified with a $1/e^2$ waist of 4 mm, an M^2 value < 1.5, and an output power of 900 mW. The output beam is sent through a polarization-independent isolator and two anti-reflection-coated telescopes to give an effective x10 beam expansion and a uniform 41 mm output beam in near-field. The transmitted beam was collimated using a shear plate and has a measured divergence at 1 km of ≈300 μrad. The average transmitted power is near 750 mW to maintain class 1 M operation. The transmit beam is directed to the center of the 279 mm Schmidt–Cassegrain receiving telescope that focuses the DIAL retrievals into a 300 μm optical fiber for detection using a fiber-coupled photo-multiplier tube.

The amplified PMT output is sampled by a 1 GS/s analog-to-digital converter. The final amplifier, optics, and telescope are fixed to an alt-azm mount for positional control of the transmitter/receiver (Tx/Rx) system. Daytime operation is enabled by the insertion of a 1.2 nm narrowband optical filter before the PMT having a >5 OD (optical density) out-of-band rejection and a filter wheel with up to 1 OD of broadband optical attenuation.

The recorded data stream was processed in real time to generate two stored records every 10 sec: one of them accumulated photon counts; the second of them accumulated voltage (proportion to the PMT current). The two channels enhance the linear detection range of the PMT to give a dynamic range of $>10^5$. In post-processing, the ten colors are separated and averaged over predetermined range bins for each record. The background points are averaged together to serve as the common reference for the signal ratios. The natural log of the DIAL derivatives over the range bins (not necessarily consecutive bins; see below) are evaluated to give the absorption line shapes of CO_2 and H_2O. The specific record used in the fit of the range-resolved concentrations depends on whether pulse pile-up error is significant in the photon count channel, in which case the current channel is used. The spectral fits were performed using a nonlinear least-squares algorithm to determine the CO_2 and H_2O concentrations at 5 min intervals. We combined these two fit results to calculate the dry-air CO_2 concentration maps. The SNR is primarily determined by the square root of the number of equivalent photons detected for the on-line signal. The size of each range bin is increased from 250 m to 500 m as the range increases from 400 m to 3 km to compensate for the inverse-square-law decrease in returned signal response.

Unlike the most common DIAL response, where the off-line backscatter returns decrease with range, R, as $\approx 1/R^2$, the backscatter returns from a plume can increase abruptly when passing through the condensate, especially for temperatures at or below freezing. The large transient responses (spikes) observed for the on-line and off-line regions at the 1.13 km range (stack position) are shown in Figure 2. This spike can cause significant discontinuities in the derivatives used to extract the power-independent concentrations which, in turn, result in rapidly changing biases for at least two of the range bins that include this condensate return. To work around this, we use a discontinued derivative approach that uses instead the two range bins on either side of the spike, thereby obtaining the CO_2 concentration increase from the plume that is devoid of distortions from this plume response. Figure 2 shows how the bins, shaded in green, are chosen to avoid the plume spike. It is also important to note that while the additional scatter from the spike causes a decrease in the downrange signal that is proportional to power, the relative decrease is independent of frequency over this narrow spectral region; therefore, the DIAL derivatives provide a true measure of the CO_2 concentration in the plume. In other words, we can recover the integrated path concentrations between any two points along the DIAL path regardless of the signal distortions from plume saturation effects.

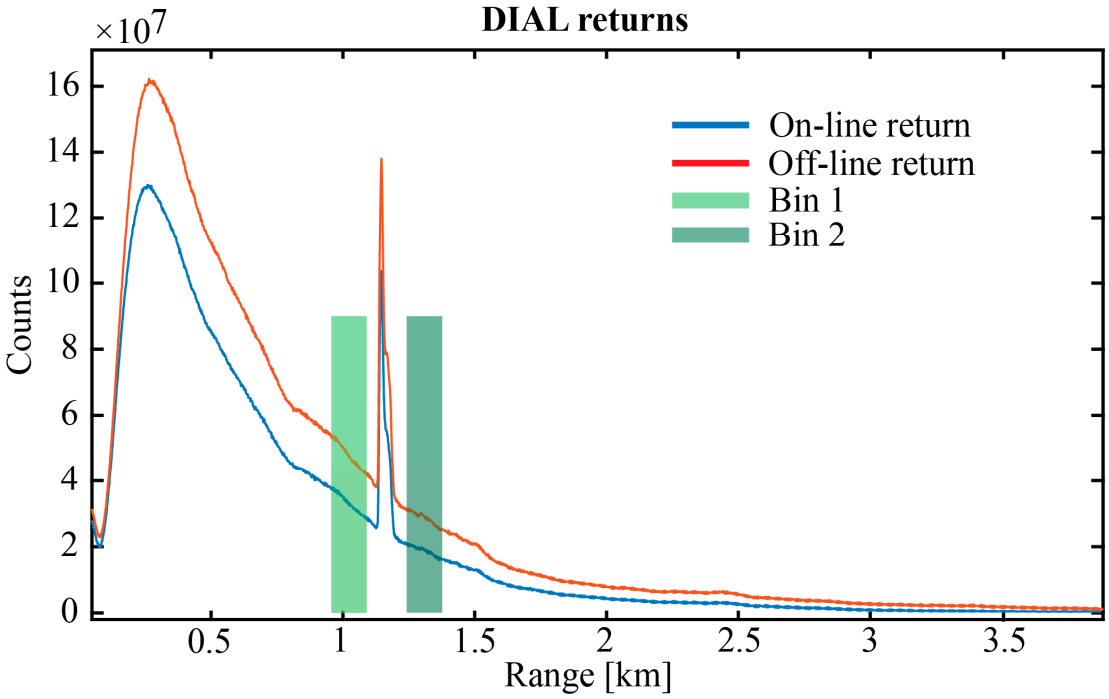

Figure 2. Raw unscaled DIAL returns from one of the on-line colors, in blue, and one of the off-line colors, in red. The spike at 1.13 km is from condensate in the plume. The bins shown with green shading were chosen to evaluate the DIAL derivatives for determination of concentration. The size of the spike is proportional to the instantaneous power at the different frequencies and therefore independent of the degree of absorption by CO_2.

2.2. Gaussian Plume Model and Tracking

The goal of this work is to compare the estimated plume emissions determined through DIAL measurements with the bottom-up CO_2 emissions derived from the natural gas burn rate of a local power plant. To achieve this, we need to both measure the concentration of CO_2 in the plume and the velocity of the plume above the stack. The latter requires knowledge of local wind velocity as well as environmental factors, such as time of day, cloud cover, ambient temperature, and power-plant-dependent variables that include exit velocity, stack height, and exit temperature. The wind data are from a local weather station (Vaisala, Model WXT536 [14]) located about two meters above the transmitter. While building interference can alter local wind conditions, the measurements near the lab are assumed to be in good agreement with the local wind at the smokestacks and are used in a Gaussian plume model to estimate the increase in the CO_2 concentration from the power plant.

To measure the emission flux from the power plant reliably, we need to consistently sample the center line of the plume that is changing with wind speed, direction, and air temperature. To solve this, we need to actively track the plume to determine the ideal position to point the DIAL system to measure plume CO_2 flux in a variety of conditions. Here, we use a Gaussian plume model [15–17] that is dependent on multiple atmospheric conditions, including temperature, solar irradiance, and wind conditions. The wind speed and direction data acquired in real time by the weather station are used to actively predict the plume location based on a running vector of the most recent 150 s of data. These predictions are then used to reposition the transceiver system every 45 s to 60 s. The tracking speed is ultimately limited by the weather station measurement time, which varies between 15 s and 45 s per record. The Gaussian plume model is used to calculate the center-line locations in 3D space, such that the beam passes through the plume at a predetermined distance away from the stack (depending on temperature; see below). The weighted average of the position vector is calculated to determine the final pointing location.

Once the best plume sampling line is calculated, the coordinates are transferred to the lab frame and offset for the transceiver base constraints (pointing 10.7° off north and platform tilt of 9°). Video of the tracking system and model is given in the Supplementary Materials.

The optimal performance of the tracking system is found in moderate winds (2 m/s to 4 m/s). Low winds lead to larger deviations between the data from the weather station and the actual conditions at the stacks located 1.13 km away, while high winds dilute the CO_2 concentration increase, making detection above ambient levels more difficult. Generally, there will be high to moderate winds during the day and early evening, and low-speed, calm conditions in the late evening and morning (see Figure A2). Additionally, while some additional scattering from the water condensate in the plume is acceptable (see Figure 2) for temperatures below freezing, the plume can become non-transparent. To compensate for changing temperatures, the distance away from the stack is varied between 30 m and 150 m depending on the density of the condensate.

2.3. Comparison with EPED Emission Data

The data reported by the EDEP plant are for consumption of natural gas (NG) fuel in pounds per hour. Methane (CH_4) makes up about 75% to 95% of NG, the balance being largely ethane (C_2H_6, < 15%) and propane (C_3H_8, < 10%). To estimate the CO_2 flow from the plant, the following mass balanced flow rate can be approximated as:

$$\dot{m}_{CO_2} = \left[\eta_{CH4}\frac{M_{CO_2}}{M_{CH_4}} + \eta_{C2H6}\frac{2M_{CO_2}}{M_{C_2H_6}} + \eta_{C3H8}\frac{3M_{CO_2}}{M_{C_3H_8}}\right]\dot{m}_{NG}\left[\frac{g}{s}\right] \quad (1)$$

where η_{CH4}, η_{C2H6}, and η_{C3H8} are the percentages by weight of methane, ethane, and propane, with methane estimated to be 77.2% of the natural gas, and the subscripted Ms designate the molar masses of CO_2, methane, ethane, and propane.

Equation (1) gives the flow rate of CO_2 from the power plant in g/s. To translate our DIAL data into a flow rate, we use the mass flux and plume area to define the flow rate [10]. The estimated flow rate of the plume can be described as:

$$\hat{\dot{m}}_{CO_2} = j_p\left[\frac{g}{m^2 s}\right]A_p\left[m^2\right] \quad (2)$$

where j_p is the mass flux of the CO_2 plume and A_p is the plume area. The plume area is calculated from the Gaussian plume model (see Appendix A). Other methods attempted, such as scanning the DIAL beam across the plume, reduced the observed increase in CO_2 below detectable levels. The sporadic nature of the plume dynamics makes this sort of classification difficult. Even with a dedicated LIDAR system for plume profiling, modeling would still be required to track the average plume center. The mass flux is defined as the product between the increase in CO_2 by the plume and the plume speed:

$$j_p = \Delta_p CO_2\left[\frac{g}{m^3}\right]u_p\left[\frac{m}{s}\right] \quad (3)$$

where u_p is the speed of the plume at the measurement location and $\Delta_p CO_2$ is the increase in CO_2 due to the plume. This can be related to the DIAL measurements using:

$$\Delta_p CO_2 = \frac{L_{DIAL}}{L_p}\Delta_{DIAL}CO_2\left[\frac{g}{m^3}\right] \quad (4)$$

where L_{DIAL} is the ≈400 m range bin, L_p is the calculated plume width parallel to the beam, and $\Delta_{DIAL}CO_2$ is the increase in CO_2 over the DIAL range bin. The speed of the plume is calculated using the weather station data and plume rise equations. With the DIAL system operating close to the plume source, the total plume speed will depend on both stack exit velocity and plume rise, as well as the average wind speed. The total wind speed is defined as:

$$u_p = \sqrt{u_z^2 + u_x^2} \quad (5)$$

where u_z is the vertical plume velocity and u_x is the downwind velocity. The downwind component is z-dependent and related to the point sensor reading using the power law:

$$u_x(z) = u_0\left(\frac{z}{z_0}\right)^{\rho} \tag{6}$$

where u_0 is the wind speed at the reading height, z_0, and the exponent, ρ, depends on atmospheric stability. To estimate the vertical plume velocity, we calculate the final plume rise height, where $u_z = 0$, and assume a linear decrease in velocity from the plume source exit velocity:

$$u_z(z) = \left(1 - \frac{z}{\Delta h}\right)u_{exit} \tag{7}$$

where u_{exit} is a constant. Details on how the plume rise is calculated are given in Appendix A. Finally, from the DIAL data and local metrological data, the calculated CO_2 flow rate, $\hat{\dot{m}}_{CO_2}$, is determined from:

$$\hat{\dot{m}}_{\mathrm{CO_2}} = \frac{L_{DIAL}}{L_p}\Delta_{\mathrm{DIAL}}\mathrm{CO_2}\sqrt{\left(1 - \frac{z}{\Delta h}\right)^2 u_{exit}^2 + u_0^2\left(\frac{z}{z_0}\right)^{2\rho}}\,A_p \tag{8}$$

The results from Equation (8) are compared to the reported EDEP emissions data below. The local wind data, u_0, are used in multiple instances, and, as such, contribute the largest source of uncertainty to both the plume tracking and plume flow-rate calculations. The full list of constants and assumptions is detailed in Appendix A.

3. Results

The DIAL measurements presented are from 10 February 2023, when an increase in CO_2 levels due to the emissions from a local power plant was well above ambient levels. The backscatter profile from 400 m to 3.3 km over the 13 h measurement period is shown in Figure 3a, where the increase in backscatter at the plume location is easily seen. To illustrate how well we track the plume, we look at the backscatter signal that shows an increase in signal return at the plume depth. After subtracting the background LIDAR returns, we can recover the total plume backscatter. Figure 3b shows the log backscatter returns at the plume, where the signal above the grey region is considered plume backscatter, showing near-continuous observation of the plume throughout the dataset. However, this also shows we miss the plume at irregular intervals, meaning that flow-rate estimates will be biased low during these less-than-ideal atmospheric conditions. The conventional CO_2 concentration map for this dataset is shown in Figure 3c, where derivatives were taken over consecutive range bins through the plume. The increase in concentration (shown in red) is clearly evident at a range of 1.13 km. However, there are multiple spots where the plume backscatter badly biases the fit concentrations, showing up as the darker red spots around the relative times of 2 h, 8 h, and 10 h, and in Figure 3b when the plume backscatter goes into the highlighted red zone.

As discussed above, we avoid this problem by performing DIAL calculations over two discontinuous range bins on either side of the plume spike, as shown in Figure 2. The measured CO_2 across the plume is shown in Figure 4a (blue) for a 13 h overnight period. For comparison, the ambient CO_2 concentrations sampled from above the lab by a cavity ringdown point sensor (CRDS) are shown in red in Figure 4a. The increases in CO_2 concentration across the plume are shown in Figure 4b for this same period after subtraction of the ambient levels determined from the average over bins downrange of the stack. The error bars from the fit residuals are shown superimposed in Figure 4 and illustrate that the CO_2 levels are consistently higher than the ambient levels. We only see up to about a 100 ppm increase in CO_2 or equivalently a maximum of 6% total absorption over the range bin. These low values minimize the impact of saturated absorption effects [18]. The error bars shown in Figure 4 range from 5 ppm to 20 ppm and are nearly independent of the overlap with the plume center.

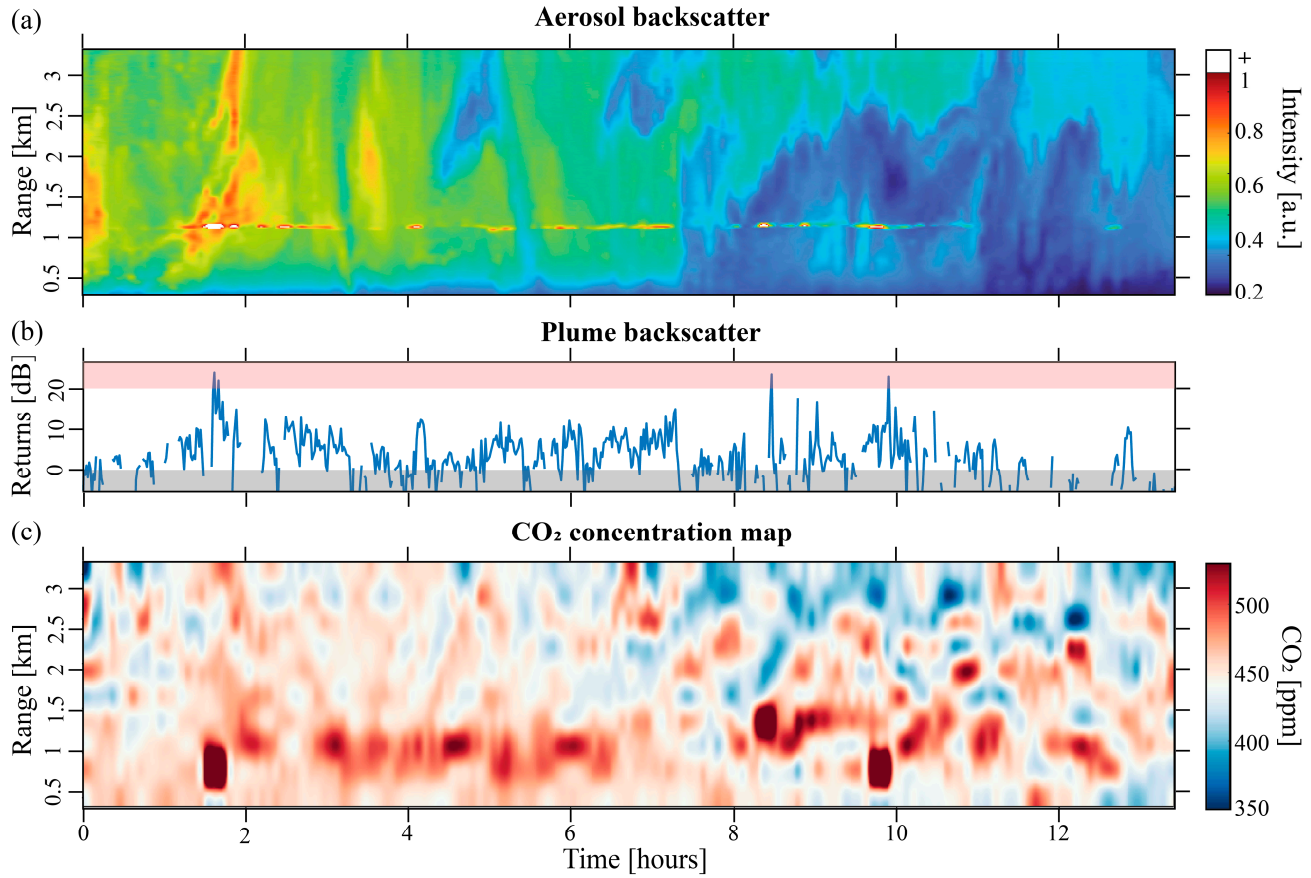

Figure 3. (**a**) The backscatter profile from one of the off-line LIDAR returns. (**b**) The log of the backscatter intensity from the plume. (**c**) The traditional range-resolved CO_2 concentration map evaluated over the 3 km range and 13 h temporal window.

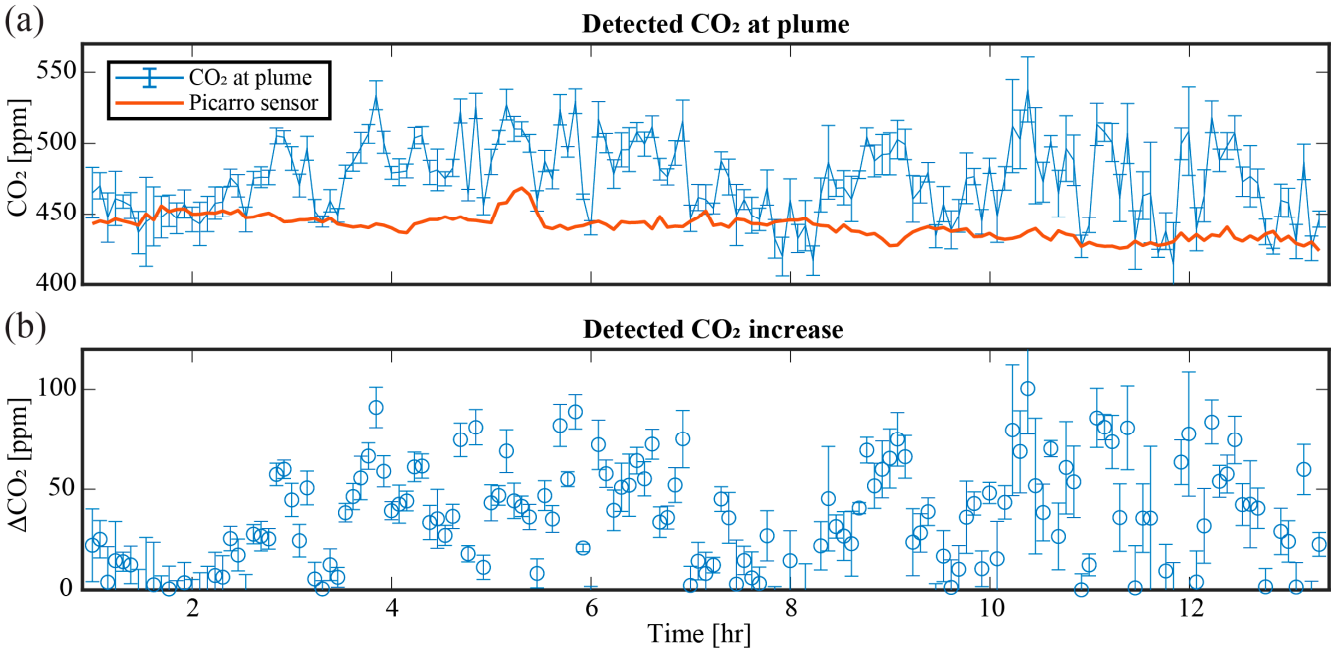

Figure 4. (**a**) The CO_2 increase in ppm over the plume region, in blue, and the ambient CO_2 levels, in red, from a CRDS instrument near the transmitter. (**b**) The overall increase in CO_2 due to the plume emissions.

4. Discussion

This measured increase in CO_2 is translated into an estimated flow rate using the process described above. The calculated values of the final plume rise, Δh, plume sampling distance, z, plume speed, u_p and plume area, A_p, used here are shown in Figure 5. The atmospheric conditions and stack parameters determine the final plume rise shown in Figure 5a. This plume rise is combined with the location of the DIAL beam relative to the stack shown in Figure 5b and the local wind speed to calculate the total plume speed shown in Figure 5c. The area of the plume used to translate the mass flux into a flow rate in Figure 5d shows large fluctuations during the first two daytime hours. These values are calculated at a 1 min resolution and then averaged to match the 5 min DIAL resolution to calculate flow rates.

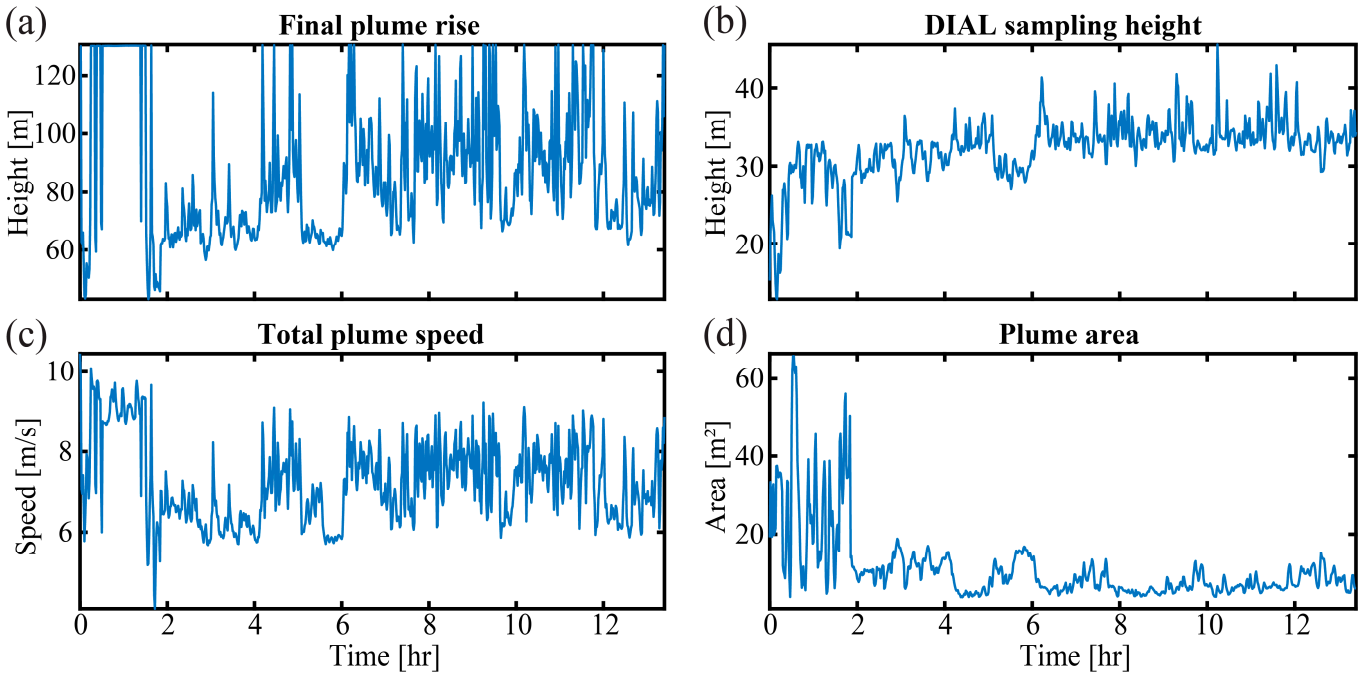

Figure 5. (**a**) The final plume rise height, (**b**) the height of the DIAL beam, (**c**) the total plume speed, and (**d**) the plume area calculated at 1 min resolution using local meteorological data.

The estimated flow rate of CO_2 is shown in Figure 6a, with values ranging from 0 g/s to 1500 g/s of CO_2 being emitted from the CU power plant with a 5 min temporal resolution. The reported EDEP data from this year (2023) were used to generate average values of the emission flux over the month of February and are shown in Figure 6b for the two side-by-side stacks at 1 h resolution. Figure 6b shows the average reported natural gas burn rate in pounds per hour for each of the two stacks, with the error bars representing the variation at each hour over the month. From these data, a small relative increase in the CO_2 flux is evident at dawn and dusk. The DIAL-based estimated CO_2 flux with 1 h resolution is shown in Figure 6c, in orange, and compared with the values from the burn rate for that day, in purple. Over the 13 h dataset, we find relatively good agreement, with nearly half of the DIAL flux predictions well within the combined uncertainties of the measured and reported data. We note that (i) the total backscatter signal decreased significantly for the latter part of the night, resulting in somewhat reduced SNR, and (ii) the periods of low wind speed can easily lead to the observed dropouts in the measured flux rate because of increased uncertainties in the predicted plume location. Nevertheless, the DIAL flux rates are seen to never exceed the reported values over the full measurement period, as expected. Gaussian plume model equations show that the CO_2 increase corresponds to an average tracking error of less than two times the z-dependent dispersion parameter, σ_z (see details in Appendix A).

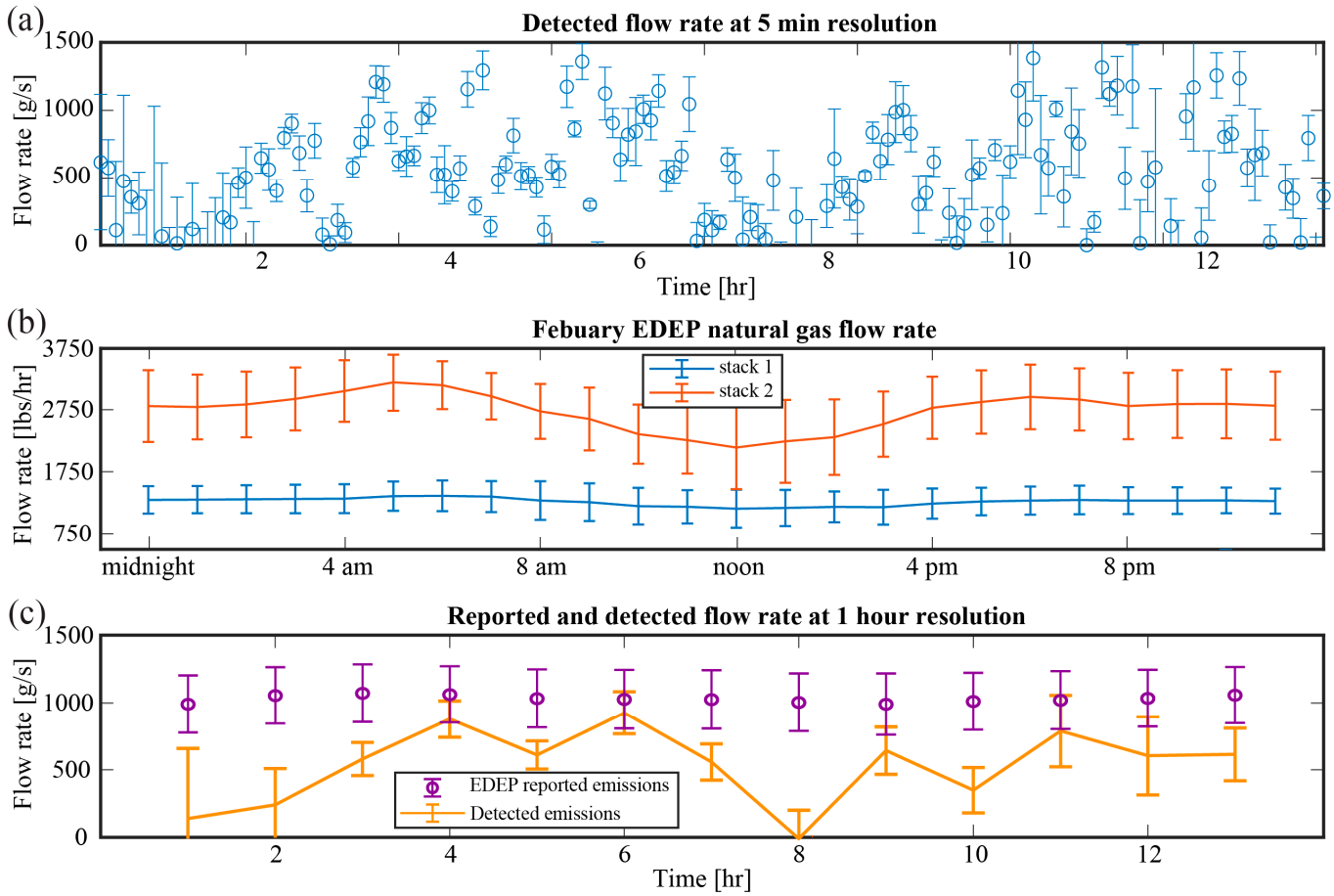

Figure 6. (**a**) The estimated flow rate using DIAL measurements and the plume model. (**b**) The plume emission rates determined from the reported natural gas usage data over the month of February 2023. (**c**) The corresponding CO_2 flow rate calculated from reported data for this day, in purple, and the rate estimated using the DIAL data and plume model, in orange.

Current efforts are directed towards incorporating real-time Doppler LIDAR data, which are expected to significantly reduce the plume model uncertainties. Unlike the current weather station location near the lab, a Doppler LIDAR system allows for range-resolved monitoring of the wind field at the plume location. As the wind speed is the largest source of uncertainty in our tracking and flow-rate estimates, reducing this error will lead to significant improvements in the flux estimates. There have been recent advances reported for systems that obtain the wind field and gas concentration simultaneously for CO_2 and CH_4 [19,20]. We note that to recover the 3D wind field, these techniques must scan over a sufficiently large area [10]. With the small concentration increases reported in this application, such scanning would quickly lower the detected plume emission below the background environment fluctuations. The robustness of measuring both the wind field and the range-resolved CO_2 concentrations with standoff techniques will be effective for many GHG source types and surrounding environments.

5. Conclusions

In this paper, we have demonstrated a compact fiber-amplifier-based DIAL system to monitor the dry-air CO_2 concentration enhancements across an emission plume from a natural gas power plant in the Boulder, Colorado, area. The DIAL system samples the spectral region at 10 different frequencies and near the highest possible repetition rate for a direct detection method. The DIAL data together with wind-field predictions from a Gaussian plume model were used to estimate the CO_2 emission flux for a 13 h nighttime period on 10 February 2023. A detailed discussion has been given of the procedure used

to actively track the plume using meteorological data sampled near the transceiver and the models used to estimate the CO_2 emission flux from this point source in an urban environment. The DIAL-derived flux was in relatively good agreement over the 13 h monitoring period with the actual emission flux determined from the reported natural gas burn rate. Underestimation bias and challenges of operating in sub-optimal atmospheric conditions have been discussed. Future work will include data from a Doppler LIDAR system to measure the 3D wind field near the stack to minimize plume tracking and model uncertainties.

Supplementary Materials: The following supporting information can be downloaded at: https://www.mdpi.com/article/10.3390/rs15174283/s1, Video S1. Video of the plume tracking including the simulated plume in the x-z plane, simulated plume in the x-y plane, images of the DIAL pointing location, and wind vectors used to calculate plume center.

Author Contributions: Conceptualization, J.R.S. and D.F.P.; methodology, J.R.S. and D.F.P.; software, J.R.S., W.J.D. and D.F.P.; validation, J.R.S. and D.F.P.; formal analysis, J.R.S., W.J.D. and D.F.P.; investigation, J.R.S. and D.F.P.; resources, J.R.S. and D.F.P.; data curation, J.R.S. and D.F.P.; writing—original draft preparation, J.R.S.; writing—review and editing, J.R.S. and D.F.P.; visualization, J.R.S.; supervision, D.F.P.; project administration, D.F.P.; funding acquisition, D.F.P. All authors have read and agreed to the published version of the manuscript.

Funding: This research received no external funding.

Data Availability Statement: Data are available at https://doi.org/10.18434/mds2-3068.

Acknowledgments: We wish to thank personnel at the University of Colorado EDEP for providing natural gas burn rate data and Kim Briggman, Marty Steven, and Pamula Chu for editorial comments and advice. We also thank Sunil Bader at NOAA for sharing the Doppler wind LIDAR data used in Appendix A. We acknowledge the support from the NIST Special Programs Office Greenhouse Gas Program and James Whetstone.

Conflicts of Interest: The authors declare no conflict of interest.

Appendix A. Gaussian Plume Model

The Gaussian plume model [16] describes how a trace gas emitter with a constant rate is spread downwind based on atmospheric conditions. The concentration at any point can be calculated using the equation:

$$C(x,y,z) = \frac{Q}{2\pi u_0 \sigma_y \sigma_z} \exp\left(-\frac{y^2}{2\sigma_y^2}\right) \exp\left(-\frac{(z-\Delta h)^2}{2\sigma_z^2}\right) \quad \text{(A1)}$$

where x is the downwind direction, y is the crosswind direction, z is the vertical direction, Q is the emission flow rate in g/s, u_0 is the wind speed, Δh is the final plume rise, and σ_z and σ_y are the plume dispersion parameters. The dispersion parameters σ_z and σ_y are x-dependent and are defined using the Pasquill stability class and net radiation index tables [15].

The final plume rise, Δh, is calculated using the following equations in stable conditions (stability classes 5–7):

$$\Delta h = 2.9\left(\frac{F}{u_0 S}\right)^{\frac{1}{3}} \quad \text{(A2)}$$

where the buoyancy flux, F, and the stability parameter, S, are defined by:

$$F = g u_{exit} r_s^2 \frac{T_s - T_a}{4T_s} \left[\frac{\mathrm{m}^4}{\mathrm{s}^3}\right] \quad \text{(A3)}$$

$$S = \frac{g}{T_a}\left(\frac{\Delta T_a}{\Delta \mathrm{z}} + 0.01\right)\left[\frac{1}{\mathrm{s}^2}\right] \quad \text{(A4)}$$

where g is the acceleration due to gravity, r_s is the smokestack radius, T_a is the atmosphere temperature, T_s is the stack temperature, and $\Delta T_a/\Delta z$ is the temperature stability. In calm conditions, with wind speeds less than 1 m/s, the plume rise is defined as:

$$\Delta h = 5\frac{F^{1/4}}{S^{3/8}} \tag{A5}$$

if the plume rise is lower than Equation (A2). In unstable and neutral conditions (stability classes 1–4), we have:

$$\Delta h = 1.6F^{1/3}x_f^{2/3}\frac{1}{u_x(\Delta h)} \tag{A6}$$

where x_f is the downwind distance of the final plume rise, calculated using the buoyancy flux as:

$$x_f = 49F^{5/8} \quad if F \leq 55\left[\frac{\mathrm{m}^4}{\mathrm{s}^3}\right] \tag{A7}$$

$$x_f = 119F^{2/5} \quad if F > 55\left[\frac{\mathrm{m}^4}{\mathrm{s}^3}\right] \tag{A8}$$

These equations determine how we track the plume and calculate the total plume speed at the DIAL sampling location. To illustrate how tracking error biases the estimated flow rate, we can modify Equation (A1) to solve the tracking error using the emission rate provided and the CO_2 increase observed at the DIAL sampling point downwind from the smokestacks.

$$\sigma_{track} = \sigma_z\sqrt{2\log\left(\frac{Q}{2\pi u_p\sigma_y\sigma_z\Delta_p CO_2}\right)} \tag{A9}$$

where σ_{track} is the tracking error, u_p is the plume velocity from Equation (5), and $\Delta_p CO_2$ is the detected CO_2 increase from the plume. Figure A1 shows the results from Equation (A9), normalized to σ_z. This shows that the level of CO_2 increase is on par with a tracking error down to 1.5 times σ_z early in the night when we see good agreement between estimated and reported flow rates.

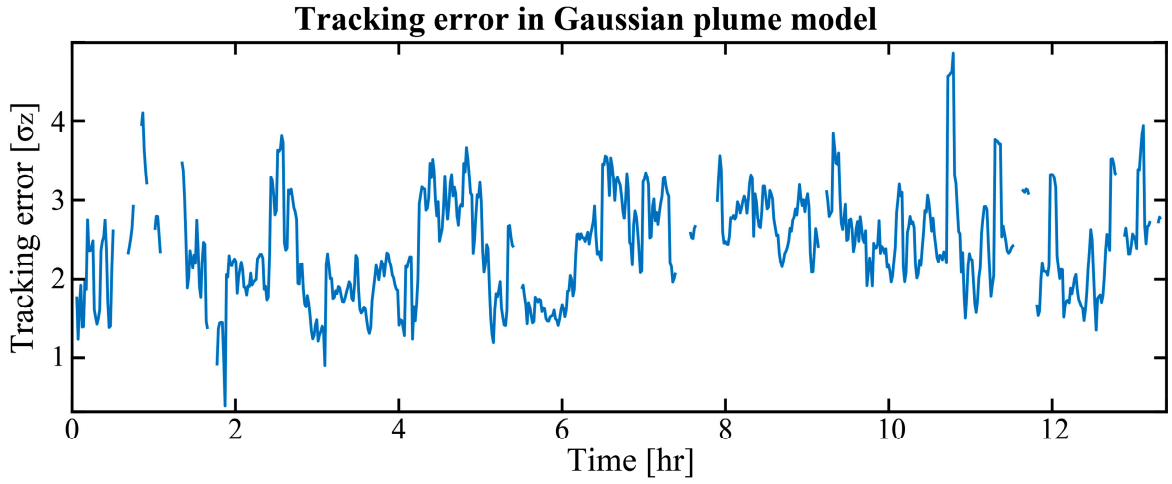

Figure A1. The tracking error calculated using a modified Gaussian plume model and reported emission data.

In addition to the weather station giving us high-temporal-resolution wind vector data, there are vertical wind vector profiles available through the National Oceanic and Atmospheric Administration (NOAA) with a 15 min temporal resolution [21]. While this is not sufficient for tracking the plume, the vertical wind profiles provide a measure of wind stability between the point sensor above the lab and the vertical profile capture a

few hundred meters away from the lab. Figure A2 shows how the two relate to each other, Figure A2a shows excellent agreement between the wind speed measurements throughout the dataset, while Figure A2b shows that the wind direction measurements are in good agreement for the first half of the dataset but show increased variability in the latter half. As expected, the lower wind speeds at night lead to increased deviation between the actual wind speed at the plume location and the measured wind speed used to track the plume and estimate the flow rate.

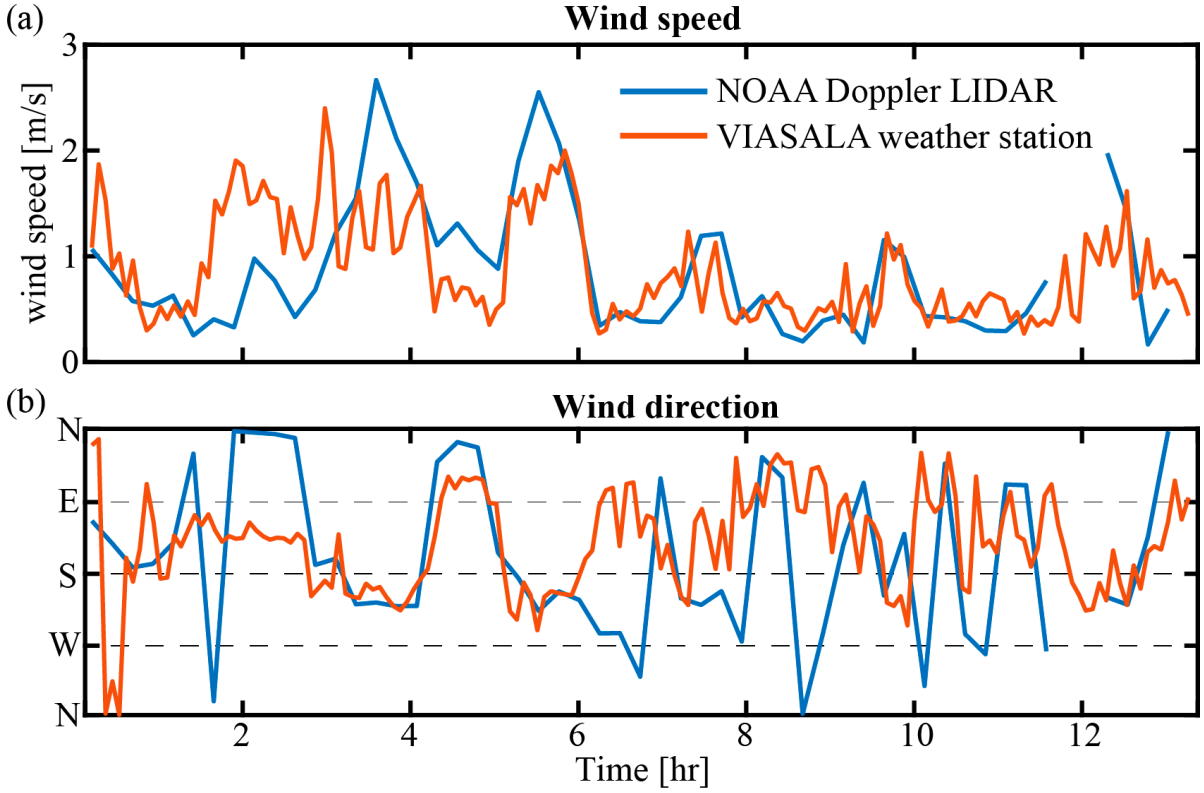

Figure A2. (**a**) The wind speed and (**b**) the wind direction measured above the lab, in red, and a few hundred meters away at the NOAA building, in blue.

Table A1. Constants used and assumptions made. Internal document: Boiler performance sheet.

Variable	Value	Source
Stack temperature	393 K	Performance sheet
Stack exit velocity	12 m/s	Performance sheet
Stack radius	0.61 m	Performance sheet
Boiler efficiency	83.5%	Performance sheet
Methane ratio	77.2%	Performance sheet
Ethane ratio	7.0%	Performance sheet
Propane ratio	1.5%	Performance sheet
Could cover	<40%	Observation
Cloud base	<2 km	Observation
Temperature stability	6 K/km	Observation

References and Note

1. Hertel, T.W.; Rose, S.K.; Tol, R.S. (Eds.) *Economic Analysis of Land Use in Global Climate Change Policy*; Routledge: New York, NY, USA, 2009; Volume 14.
2. Gimmestad, G.G. *Differential-Absorption Lidar for Ozone and Industrial Emissions*; Springer: New York, NY, USA, 2005.
3. Orr, B.J. Infrared LIDAR applications in atmospheric monitoring. In *Encyclopedia of Analytical Chemistry: Applications, Theory and Instrumentation*; New York, NY, USA: Wiley, 2006; pp. 1–9.

4. Ehret, G.; Bousquet, P.; Pierangelo, C.; Alpers, M.; Millet, B.; Abshire, J.B.; Bovensmann, H.; Burrows, J.P.; Chevallier, F.; Ciais, P.; et al. MERLIN: A French-German Space Lidar Mission Dedicated to Atmospheric Methane. *Remote Sens.* **2017**, *9*, 1052.
5. Baldocchi, D.; Falge, E.; Gu, L.; Olson, R.; Hollinger, D.; Running, S.; Anthoni, P.; Bernhofer, C.; Davis, K.; Evans, R.; et al. FLUXNET: A new tool to study the temporal and spatial variability of ecosystem-scale carbon dioxide, water vapor, and energy flux densities. *Bull. Am. Meteorol. Soc.* **2001**, *82*, 2415–2434.
6. Lin, J.C.; Gerbig, C.; Wofsy, S.C.; Andrews, A.E.; Daube, B.C.; Grainger, C.A.; Stephens, B.B.; Bakwin, P.S.; Hollinger, D.Y. Measuring fluxes of trace gases at regional scales by Lagrangian observations: Application to the CO_2Budget and Rectification Airborne (COBRA) study. *J. Geophys. Res. Atmos.* **2004**, *109*, D15304. [CrossRef]
7. Thoma, E.D.; Shores, R.C.; Thompson, E.L.; Harris, D.B.; Thorneloe, S.A.; Varma, R.M.; Hashmonay, R.A.; Modrak, M.T.; Natschke, D.F.; Gamble, H.A. Open-Path Tunable Diode Laser Absorption Spectroscopy for Acquisition of Fugitive Emission Flux Data. *J. Air Waste Manag. Assoc.* **2005**, *55*, 658–668. [CrossRef] [PubMed]
8. Hashmonay, R.A.; Yost, M.G.; Mamane, Y.; Benayahu, Y. Emission rate apportionment from fugitive sources using open-path FTIR and mathematical inversion. *Atmos. Environ.* **1999**, *33*, 735–743. [CrossRef]
9. Robinson, R.A.; Gardiner, T.D.; Innocenti, F.; Finlayson, A.; Woods, P.T.; Few, J.F.M. First measurements of a carbon dioxide plume from an industrial source using a ground based mobile differential absorption lidar. *Environ. Sci. Process. Impacts* **2014**, *16*, 1957–1966. [CrossRef] [PubMed]
10. Yue, B.; Yu, S.; Li, M.; Wei, T.; Yuan, J.; Zhang, Z.; Dong, J.; Jiang, Y.; Yang, Y.; Gao, Z.; et al. Local-Scale Horizontal CO_2 Flux Estimation Incorporating Differential Absorption Lidar and Coherent Doppler Wind Lidar. *Remote Sens.* **2022**, *14*, 5150. [CrossRef]
11. Stroud, J.R.; Plusquellic, D.F. Range resolved CO_2 measurements over 3 km using a 10-point fiber-based differential-absorption LIDAR (DIAL) system. In *CLEO: Applications and Technology*; Optica Publishing Group: Washington, DC, USA, 2022; p. AM2K-3.
12. Wagner, G.A.; Plusquellic, D.F. Plusquellic. Multi-frequency differential absorption LIDAR system for remote sensing of CO_2 and H_2O near 1.6 μm. *Opt. Express* **2018**, *26*, 19420–19434. [CrossRef] [PubMed]
13. Univrsity of Colorado (CU) East District Energy Plant (EDEP). Available online: https://www.colorado.edu/fmenergy/contacts (accessed on 13 April 2023).
14. Certain commercial equipment, instruments, or materials are identified in this paper in order to specify the experimental procedure adequately. Such identification is not intended to imply recommendation or endorsement by NIST, nor is it intended to imply that the materials or equipment identified are necessarily the best available for the purpose
15. Turner, D.B. A diffusion model for an urban area. *J. Appl. Meteorol. Climatol.* **1964**, *3*, 83–91. [CrossRef]
16. Briggs, G.A. Some Recent Analyses of Plume Rise Observations. Available online: https://repository.library.noaa.gov/view/noaa/33598 (accessed on 13 April 2023).
17. Brusca, S.; Famoso, F.; Lanzafame, R.; Mauro, S.; Garrano, A.M.C.; Monforte, P. Theoretical and Experimental Study of Gaussian Plume Model in Small Scale System. *Energy Procedia* **2016**, *101*, 58–65. [CrossRef]
18. Dherbecourt, J.-B.; Melkonian, J.-M.; Godard, A.; Lebat, V.; Tanguy, N.; Blanchard, C.; Doz, S.; Foucher, P.-Y.; Huet, T.; Watremez, X.; et al. NAOMI GAZL: A Multispecies DIAL Tested on the TADI Gas Leak Simulation Facility. In *EPJ Web of Conferences*; EDP Sciences: Hefei, China, 2020; Volume 237, p. 03016.
19. Koch, G.J.; Barnes, B.W.; Petros, M.; Beyon, J.Y.; Amzajerdian, F.; Yu, J.; Davis, R.E.; Ismail, S.; Vay, S.; Kavaya, M.J.; et al. Coherent differential absorption lidar measurements of CO_2. *Appl. Opt.* **2004**, *43*, 5092–5099. [CrossRef] [PubMed]
20. Cezard, N.; Le Mehaute, S.; Le Gouët, J.; Valla, M.; Goular, D.; Fleury, D.; Planchat, C.; Dolfi-Bouteyre, A. Performance assessment of a coherent DIAL-Doppler fiber lidar at 1645 nm for remote sensing of methane and wind. *Opt. Express* **2020**, *28*, 22345–22357. [CrossRef]
21. Atmospheric Remote Sensing, NOAA Chemical Science Laboratory. Available online: https://csl.noaa.gov/groups/csl3/measurements/dsrc/dalek02/ (accessed on 1 May 2023).